Michigan Technological University

Digital Commons @ Michigan Tech

Dissertations, Master's Theses and Master's Reports

2021

Investigating ice nucleation at negative pressures using molecular dynamics: A first order approximation of the dependence of ice nucleation rate on pressure

Elise Rosky
Michigan Technological University, emrosky@mtu.edu

Copyright 2021 Elise Rosky

Recommended Citation

Rosky, Elise, "Investigating ice nucleation at negative pressures using molecular dynamics: A first order approximation of the dependence of ice nucleation rate on pressure", Open Access Master's Thesis, Michigan Technological University, 2021.
https://doi.org/10.37099/mtu.dc.etdr/1303

Follow this and additional works at: https://digitalcommons.mtu.edu/etdr

 Part of the Atmospheric Sciences Commons, and the Atomic, Molecular and Optical Physics Commons

INVESTIGATING ICE NUCLEATION AT NEGATIVE PRESSURES USING MOLECULAR DYNAMICS: A FIRST ORDER APPROXIMATION OF THE DEPENDENCE OF ICE NUCLEATION RATE ON PRESSURE

By

Elise Rosky

A THESIS

Submitted in partial fulfillment of the requirements for the degree of

MASTER OF SCIENCE

In Physics

MICHIGAN TECHNOLOGICAL UNIVERSITY

2021

© 2021 Elise Rosky

This thesis has been approved in partial fulfillment of the requirements for the Degree of MASTER OF SCIENCE in Physics.

Department of Physics

Co-advisor: *Dr. Raymond Shaw*

Co-advisor: *Dr. Will Cantrell*

Committee Member: *Dr. Issei Nakamura*

Department Chair: *Dr. Ravindra Pandey*

Contents

List of Figures

List of Tables

Acknowledgments

I would like to thank my research advisors Dr. Raymond Shaw and Dr. Will Cantrell for their constant support and guidance, and for helping to open many doors of opportunity.

I would like to thank Dr. Tianshu Li, at George Washington University, for being a collaborator on this work and lending enormous insight on the field of molecular dynamics simulations. His contributions greatly enhance the impact of this work.

We are grateful to Dr. Issei Nakamura and the LAMMPS community for helpful discussions.

Research reported here was supported in part by funding provided by the National Aeronautics and Space Administration (NASA), under award number 80NSSC20M0124, Michigan Space Grant Consortium (MSGC). Funding from NSF grants AGS-1541998 and AGS-2019649 is gratefully acknowledged. Li acknowledges the support by NSF through award CBET-2053330.

List of Abbreviations

MD	Molecular Dynamics
FFS	Forward Flux Sampling
CNT	Classical Nucleation Theory

Abstract

Atmospheric scientists and climate modelers are faced with uncertainty around the process of ice production in clouds. While significant progress has been made in predicting homogeneous and heterogeneous ice nucleation rates as a function of temperature, recent experiments have shown that ice nucleation rates can be enhanced without decreasing temperature, through various mechanical agitations. One hypothesis for these findings is that mechanisms of stretching water and thereby inducing negative pressure in the liquid could lead to an increase in freezing rate. To better understand the viability of this concept, the effect of negative pressure on ice nucleation rates needs to be explored.

To that end, we have conducted molecular dynamics simulations of water at negative pressures. Homogeneous ice nucleation rates for the ML-mW and mW water models are evaluated at pressures ranging from atmospheric to -1000 atm, using Forward Flux Sampling and constant cooling simulations. We find that the density difference between ice and liquid water is central in determining the increase in nucleation rate with negative pressure. With these results, we analyze an equation that has been posed as a first order approximation to quantify how nucleation rate changes with negative pressure. The equation predicts the slope of lines of constant nucleation rate in temperature–pressure coordinates, shining a light on the importance of the water

density anomaly in determining the slope. We conclude that this linear approximation works well for the mW and ML-mW water models and can be useful in making experimental predictions to advance the study of ice nucleation mechanisms.

Chapter 1

Introduction

The physics governing the phase transition from liquid water to ice is still under investigation. Molecular dynamics (MD) simulations of ice nucleation on the molecular scale are helpful in revealing the fundamental mechanisms involved in ice formation. This topic is relevant to understanding ice formation in clouds, and efforts to control freezing through enhancing or suppressing ice nucleation [3, 4]. Homogeneous ice nucleation occurs in supercooled water when an ice cluster of critical radius forms, overcoming the Gibbs free energy barrier imposed by the surface energy of the cluster, without catalysis from any impurities or container walls. The ice nucleation rate coefficient, J, is the number of critical clusters forming per unit volume and time. The nucleation rate increases as the temperature is lowered further from the melting point. In this study, we aim to understand how negative pressures (negative valued diagonal components of the stress tensor) within the liquid influence ice nucleation rates.

Experiments and everyday experience show that various processes can help supercooled liquid overcome the free energy barrier and catalyze ice nucleation. Introducing certain impurities, or shaking or agitating the water are examples [5, 6]. The explanation for the latter observations is still unclear. In controlled lab experiments, only certain types of mechanical agitation are effective at catalyzing ice formation [7, 8]. Experiments show that moving the contact line of a water droplet across its substrate only triggers ice nucleation when combined with stretching/distorting of the contact line [2]. This finding indicates that the water surface plays an important role

and points to a possible contribution from Laplace pressure, which arises from curved liquid-vapor interfaces. A concave surface has a negative radius of curvature and results in negative Laplace pressure. Just as the melting temperature of water increases under negative pressures [9], ice nucleation rates also increase due to a lowering of the Gibbs free energy barrier. Therefore, it's possible that negative pressure/stress perturbations imposed on a supercooled liquid droplet can increase the ice nucleation rate while maintaining a constant temperature. This and other possible sources of negative pressure in atmospheric water droplets are discussed in Marcolli et al. [1] and Yang et al. [10]. The atmospheric science community has been predominately focused on the temperature dependence of ice nucleation. This work, in contrast, is another step in exploring the role that pressure changes might play.

We use molecular dynamics to explore the relative roles of temperature and pressure on ice nucleation; specifically, for the range of pressures expected in experimental and atmospheric scenarios [10]. Li et al. [11], Yang et al. [7], and others have proposed that a Clausius-Clapeyron-like relation can be used to express the equivalence between temperature and pressure in achieving a given nucleation rate:

$$p(T) = p_0 + \frac{l_f}{T_m \Delta v_{ls}}(T - T_0), \tag{1.1}$$

where p_0 and T_0 are known reference pressure and temperature values for a nucleation

rate coefficient of interest. In this study we take atmospheric pressure as the reference. The molar volume difference between liquid and ice, Δv_{ls}, is negative in the pressure regime considered in this study, a phenomenon known as the water density anomaly. The variable l_f is the latent heat of fusion and T_m is the melting temperature, both at p_0. In subsequent sections, we will outline the derivation of this approximation and evaluate the extent to which it provides a reasonable prediction of the nucleation rate in pressure–temperature coordinates.

Freezing of water at negative pressures lacks both simulated and experimental data. Roedder [9] took measurements of the melting temperature of water at negative pressures, but to our knowledge, no experimental assessment of homogeneous freezing rates at negative pressures has been conducted. Evidence for an increase in ice nucleation rates at negative pressures is found by extrapolating experimental data at positive pressures into the negative pressure regime [1], and is also implied by Classical Nucleation Theory (CNT). A recent study by Bianco et al. used molecular dynamics simulations to explore ice nucleation rates in the TIP4P/Ice water model at negative pressures [12]. Their work explores anomalous behaviors that occur in water in the negative pressure regime, and reports nucleation rates using seeding, an approximate method that reproduces rigorous techniques by combining molecular dynamics simulations with CNT.

In this study, we consider two coarse-grained water models that are commonly used to

explore ice nucleation due to their computational efficiency: ML-mW and the original mW model. The mW model was introduced by Molinero et al. [13] and is designed to represent the physics of the freezing process while maintaining computational efficiency. The mW model is a coarse grained model, modeling each water molecule as a single atom. Based on the Stillinger-Weber potential, the mW model simulates the effects of hydrogen bonds by imposing a three-body potential that is felt between each group of three mW molecules, favoring tetrahedral angles. There is also a two-body potential that exists between each pair of mW molecules. The ML-mW model was created by further optimizing the mW model parameters using machine learning with properties of real water as a target [14]. If the approximation given by Equation 1.1 is valid, it suggests the density anomaly plays a central role in determining the slope of lines of constant nucleation rate in pressure–temperature space. The molar volume difference upon melting, Δv_{ls}, has undergone great improvement in the ML-mW model compared to the original mW model. The experimental value for Δv_{ls} at 1 atm and 273 K is -1.61 cm^3 mol^{-1}, which the ML-mW model reproduces with much more fidelity than the original mW model, giving -1.38 and -0.42 respectively [14]. These two water models, which exhibit significantly different density anomalies, provide useful contrasts to assess the validity of Equation 1.1 and explore the dependence of nucleation rates on pressure. We propose that the improvement to Δv_{ls} results in a more accurate representation of the homogeneous freezing line, $(dp/dT)_{J=const}$.

Chapter 2

Constant nucleation rate lines from simulations

The results presented in this Chapter were obtained in collaboration with Tianshu Li. Methods and simulations described in Sections 2.2 and 2.3 were performed by Tianshu Li. The work is in review at Chemical Physics Letters as the following reference.

> Rosky, E., W. Cantrell, T. Li, R. Shaw. "Homogeneous ice nucleation rate at negative pressures: The role of the density anomaly." Chemical Physics Letters, in review.

We investigate the homogeneous ice nucleation rate coefficients of the mW and ML-mW water models at 1, -500, and -1000 atm. Most studies of ice nucleation and water model properties have been conducted at 1 atm, so inclusion of this pressure allows us to compare and validate our results with other studies. The -500 atm and -1000 atm values were chosen to be within the negative Laplace pressure range that could account for enhanced nucleation rates observed in experiments [2]. The selected pressures remain in the regime where the molar volume of ice is larger than liquid water, $\Delta v_{ls} < 0$. The sign of Δv_{ls} is a crucial factor when studying the behavior of homogeneous freezing with respect to pressure.

We use two approaches to obtain nucleation rates. In the first method, we obtain nucleation rates from direct simulations of homogeneous ice nucleation at negative pressures. We do this by repeating constant cooling rate simulations many times at a

fixed pressure. This approach is akin to experimental methods of measuring ice nucleation rates. The second method obtains nucleation rates in a range of temperatures and (negative) pressures using forward flux sampling (FFS) [15] at constant temperature. These two approaches are complementary and allow us to explore a broad range of nucleation rates. They are also more direct than the methods commonly used in MD studies, where nucleation rates are derived using precise calculation of thermodynamic properties combined with expressions from classical nucleation theory [12, 16]. The methods used in our study do not rely on CNT, thus we are able to compare the results of our simulations with theoretical expressions. In our analysis, we compare the slope of our constant nucleation rate lines with theoretical predictions from Equation 1.1.

2.1 Constant cooling rate simulations

LAMMPS [17] is used to conduct the molecular dynamics simulations. For the constant cooling rate simulations, a simulation box containing 4,096 coarse-grained water molecules is first equilibrated at the starting temperature. The temperature range that the system is cooled through differs for each pressure and between the models. The temperature range in each case is selected so that ice nucleation is extremely likely to occur during the linear cooling process at the cooling rate chosen. For the mW model the temperature ranges are 215 K to 195 K at 1 atm and -500 atm; and

215 K to 200 K at −1000 atm. For the ML-mW model the ranges are 225 K to 205 K at 1 atm; 230 K to 210 K at −500 atm; and 230 K to 215 K at −1000 atm. The constant cooling rate simulations are conducted in an isenthalpic (NPH) ensemble coupled with a thermostat and with periodic boundary conditions employed. After equilibration at the initial temperature, the system is cooled at rate of 0.25 K/ns. Johnston et al reported that a cooling rate of 1 K/ns is the highest cooling rate one can use to still observe crystallization in mW model nanodroplets containing 13,824 molecules [18]. We found that at lower pressures, *e.g.*, −1000 atm, lower cooling rates were needed to observe crystallization. For the ML-mW, 16% of our trajectories at −1000 atm did not crystallize. This is marked by a very gradual, linear increase in ice-like fraction during cooling with the final ice fraction not reaching 0.8. These runs were not included in the data on ice nucleation phase transition.

The phase of the system is monitored using the q_6 order parameter with a cutoff distance of 3.5 Angstroms [19]. Figure 2.2 shows how this order parameter evolves for each atom in the volume of water as the system freezes. A molecule with q_6 order parameter greater than 0.54 is considered an ice-like molecule and is colored blue in Figure 2.2 while atoms with q_6 value smaller than the 0.54 threshold are considered liquid-like and are shaded in red. This threshold was determined by measuring the distribution of order parameters in a box of pure ice, and selecting a threshold value just outside that range. The threshold we have chosen is the same for both ML-mW and mW models and is consistent with the threshold used in other studies [20]. To

determine the freezing temperature of a single cooling run, we look at the ratio of ice-like molecules to total molecules as a function of time, which is equivalent to a function of temperature because the system is being cooled at a constant rate. When the system freezes, the fraction of ice-like molecules steeply increases and plateaus at around 0.8. We fit a sigmoidal curve, $F(t) = A/(1 + \exp(-B(x - C))) - D$, to the data and specify the freezing temperature to be the inflection point of the sigmoid. A, B, C, and D are fitting parameters that represent the maximum ice fraction, speed of transition, inflection point, and vertical shift, respectively. Figure 2.1 is an example evolution of the N_{ice}/N_{total} ratio for one constant cooling ramp simulation run. The figure shows the raw data, the sigmoidal fit, and the nominal freezing temperature.

The sigmoidal fits for all the simulation trajectories for the ML-mW model can be seen in the top panel of Figure 2.3. At each pressure, 30-50 cooling trials are run to gather a distribution of freezing temperatures, and the resulting temperature distributions are shown in the bottom panel of Figure 2.3.

In Chan et al., the ML-mW water is cooled at a rate of 0.5 K/ns at 1 atm, and ice nucleation occurs at 210 K [14]. With our slower cooling rate of 0.25 K/ns, we observe that ice nucleation in ML-mW occurs at a higher temperature of 215 K. As anticipated, Figure 2.3 shows that homogeneous ice nucleation occurs at higher temperatures when the system is under more negative pressures. This is seen to be the case for both water models, with the ML-mW exhibiting a larger increase than

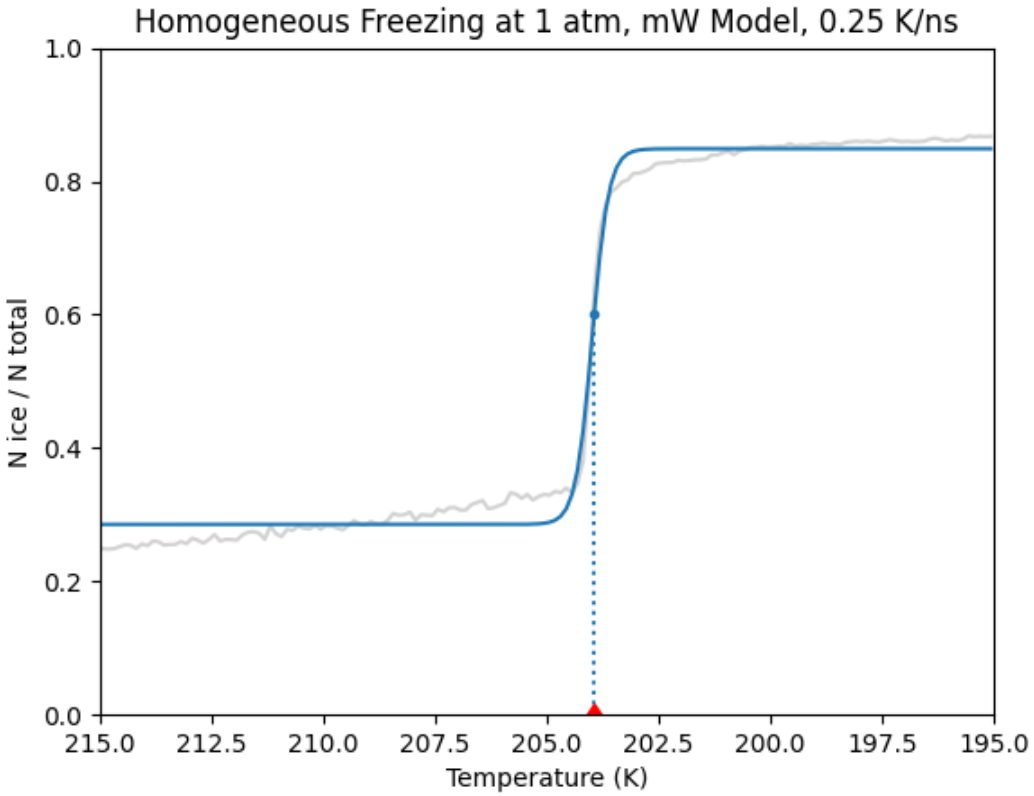

Figure 2.1: An example of one freezing trajectory at 1 atm. The grey line shows the raw data of ice fraction. The colored line is a sigmoid fit to the data. The blue dot indicates the inflection points that is used as the nominal freezing temperature for each run, the dashed line and red marker are a guide for the eye.

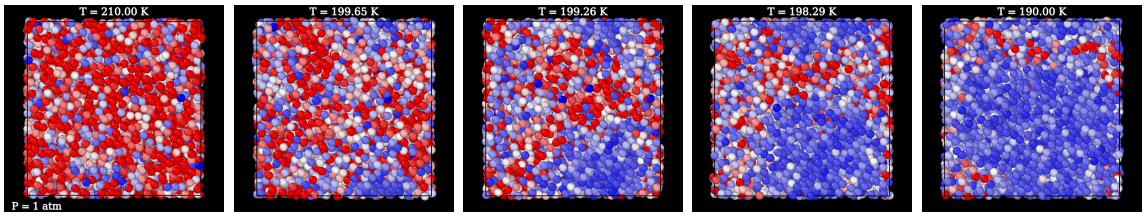

Figure 2.2: Snapshots from a representative constant cooling simulation where homogeneous freezing occurs in the mW model. The coloring indicates the value of the q_6 order parameter, with blue shades denoting molecules with ice-like q_6 order parameter greater than 0.54 and red shades denoting liquid-like order parameter.

the original mW.

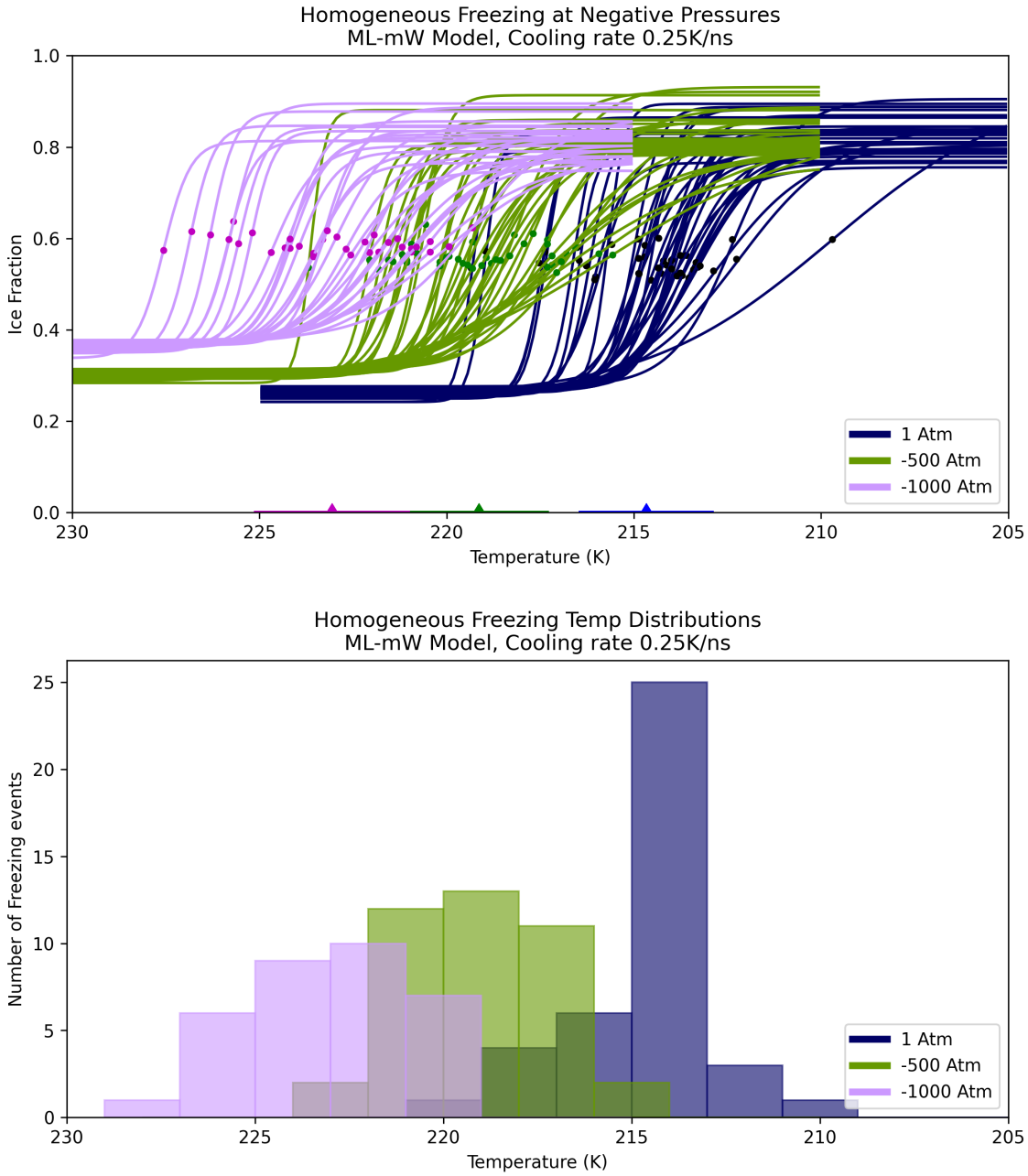

Figure 2.3: Top: All freezing trajectories for the ML-mW model at three different pressures. The dots indicate the inflection point that is used as the nominal freezing temperature for each run. The markers on the abscissa denote the average freezing temperature for each pressure, and the standard deviation. Bottom: Distribution of nucleation events, used to calculate nucleation rates

The freezing temperature distributions in the bottom panel of Figure 2.3 are used to calculate nucleation rate coefficients in these temperature ranges using the method described by Zobrist et al [21]. We count the number of freezing events that occur in evenly spaced temperature intervals centered at temperatures T_i. Next, the total observation time in each temperature interval, $t_{tot,i}$, is calculated as the sum of the contributions from the simulation runs that remained liquid over the entire temperature interval and the runs that freeze. Once a run freezes, the remaining time spent in that temperature interval is not counted in the observation time. We obtain the average homogeneous ice nucleation rate (s^{-1}) at the mean temperatures T_i by dividing the total number of freezing events in that internal by $t_{tot,i}$. In order to obtain the nucleation rate coefficient ($s^{-1}m^{-3}$) from this, we divide by the volume of the simulation box. Figure 2.4 shows the uncertainty on the nucleation rate coefficient calculations using two temperature bins. The lower and upper error bounds with a confidence level of 0.99 are found using Koop et al, Equations 13(a,b) [22].

The nucleation rate coefficients observed via constant cooling rate simulations are confined to a certain observable range, limited by the chosen cooling rate and volume of water. The calculated nucleation rate coefficients for each pressure are on the order of 10^{32} and 10^{33} $s^{-1}m^{-3}$. This method of cooling a water 'sample' many times is similar to the way that freezing temperature measurements are often conducted experimentally [21, 23, 24, 25], albeit that the sample volume in these simulations (1.3×10^{-19} cm^3) is much smaller than in experiments and the cooling rate is much

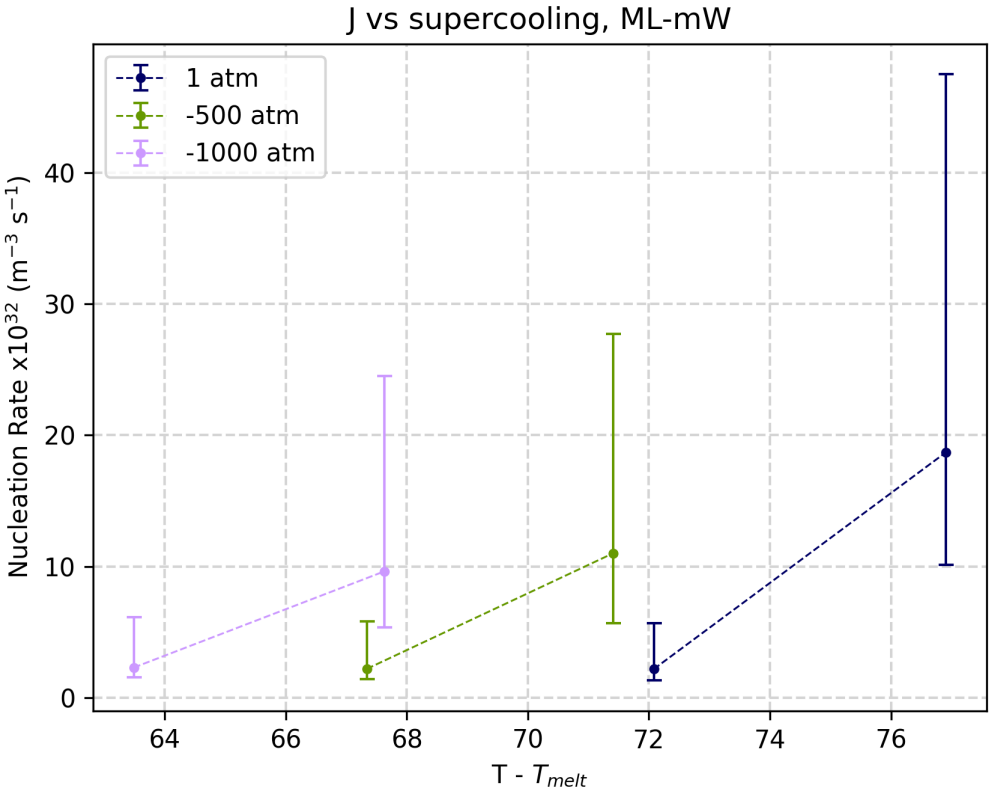

Figure 2.4: Nucleation rate coefficients calculated from constant cooling rate simulations, with upper and lower bounds.

faster. As a result, the nucleation rate coefficients accessible to this approach falls far beyond experimental range. This gap can be closed by the forward flux sampling approach, as discussed in Section 2.2.

Figure 2.5 shows the pressure versus temperature dependence of the $J = 10^{32}$ s^{-1} m^{-3} line (triangles) for both the mW and ML-mW models plotted along with the equilibrium melting point line (circles). There is 99% certainty that the $J = 10^{32}$ s^{-1} m^{-3} line lies within the shaded region [22]. The data points for the melting-point line are obtained by using the direct-phase coexistence method at each pressure, where

the melting temperature is taken as the lowest temperature at which the system completely melts [26, 27]. The grey solid line is the experimental melting point line extrapolated to negative pressures [1]. For both models, water melts at higher temperatures when the pressure is negative in accordance with the Clausius-Clapeyron relation. The qualitative behavior of the ML-mW melting point line is in good agreement with the extrapolation from experimental measurements. It is worth noting that the ML-mW melting temperature obtained using this method is greater than what was reported in Chan et al [14] by 3 K. Appendix A provides further details about the equilibrium melting point data.

2.2 Forward Flux Sampling

To gain a more complete understanding of the p, T dependence of nucleation rate, we also calculate the nucleation rate coefficients of the ML-mW model for a range of pressures and temperatures using Forward Flux Sampling (FFS) [15]. FFS enables a direct calculation of nucleation rate coefficient covering a wide range of thermodynamic conditions, particularly those where nucleation rate becomes too small to be obtained by standard MD simulation. More importantly, since FFS does not rely on any nucleation theory, the method can be used independent of CNT. Indeed, FFS has been successfully employed to study homogeneous ice nucleation based on both mW model [28, 29] and TIP4P/Ice model [30].

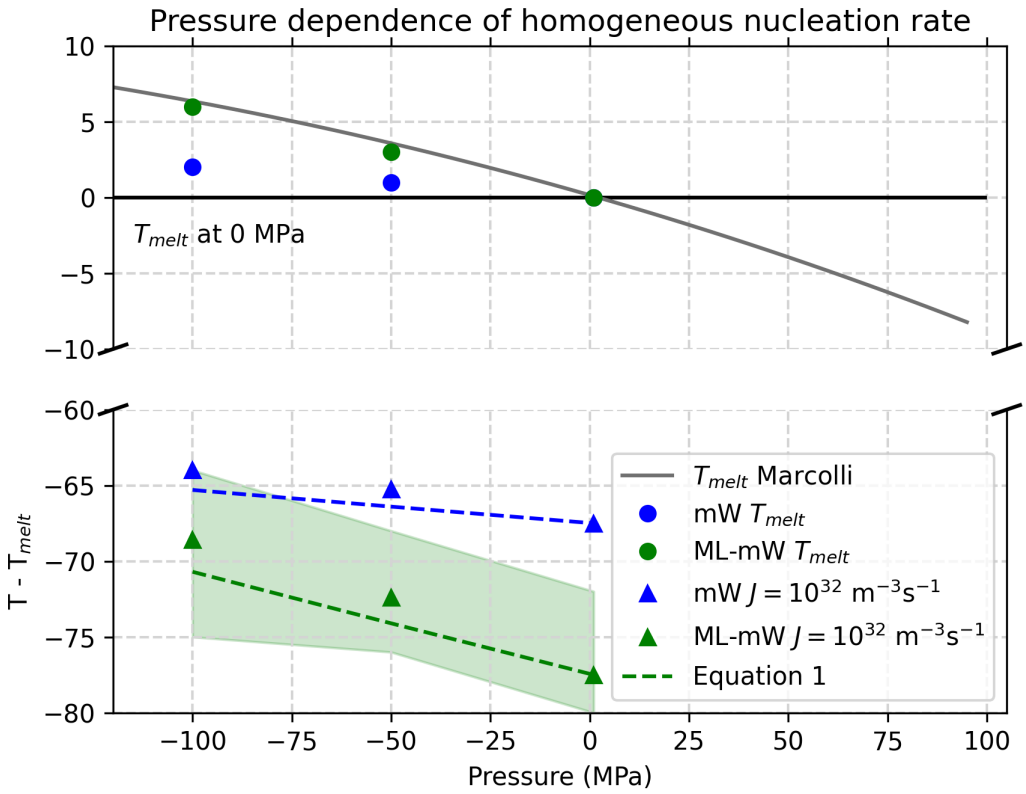

Figure 2.5: 'Phase diagram' showing the pressure and temperature dependence of the equilibrium melting point and line of constant nucleation rate coefficient $J = 10^{32}$ m^{-3}s^{-1}. Circles are the melting temperatures for the mW water model (blue) and ML-mW model (green), while the grey line is the experimental melting point line extrapolated to negative pressures [1]. Triangles denote our simulation results for homogeneous nucleation rate coefficient at negative pressures. The dashed lines are theoretical predictions given by Equation 1.1 from Yang et al [2]. The simulation results obtained at 1 atm are used as the reference values (p_0, T_0) for Equation 1.1. The origin of the y-axis is set as the melting temperature, T_{melt} at 1 atm.

Here we carry out FFS calculation using our recent implementation to compute homogeneous ice nucleation rate coefficients for the p, T range from -1000 atm to 1 atm and 222 K to 250 K, respectively. Under the framework of FFS [15], the rate constant R is given by $R = \dot{\Phi}_{\lambda_0} \prod_{i=0}^{n} P(\lambda_i|\lambda_{i-1})$, where $\dot{\Phi}_{\lambda_0}$ is the flux rate crossing the first interface λ_0, and $P(\lambda_i|\lambda_{i-1})$ is the probability for a trajectory starting from

the interface λ_{i-1} and successfully reaching the next interface λ_i. The interface λ_i is defined by the order parameter λ, which is the number of ice-like water molecules, characterized by a local bond-order parameter $q_6 > 0.5$, within the largest ice cluster [28]. For ice nucleation based on the mW model, such an order parameter has been demonstrated to effectively reflect the actual reaction coordinates of ice nucleation [31, 32, 33]. Given the similarity between the mW and ML-mW models, we thus expect this order parameter is equally applicable to the current study. The initial flux rate $\dot{\Phi}_{\lambda_0}$ is obtained through dividing the number N of direct crossings to the first interface λ_0 from liquid basin (~ 200) by the product of the total simulation time t of this step and the simulation volume V, namely, $\dot{\Phi}_{\lambda_0} = N/(tV)$. Using the collected configurations at the interface λ_0, we then consecutively fire a large number of shootings M_{i-1} at each interface λ_{i-1} and collect N_{i-1} (~ 120) configurations that successfully cross the next interface λ_i, to compute the crossing probability $P(\lambda_i|\lambda_{i-1}) = N_{i-1}/M_{i-1}$. The typical error bar of the computed nucleation rate coefficient is within $75 \sim 90\%$ of the absolute rate [11]. To further enhance the accuracy of the calculated rate coefficients, we conduct three independent FFS runs for each p, T condition, through which the final rate is obtained by a geometric average of the calculated rates, *i.e.*, $R(p,T) = \left(\prod_{j=1}^{3} R_j\right)^{1/3}$. The convergence of FFS calculations with respect to the number of configurations (N_i) collected at each interface λ_i has been carefully checked as described in Appendix B.

The FFS calculations cover a wide range of ice nucleation rate coefficients, from 10^8

$s^{-1}m^{-3}$ to 10^{33} $s^{-1}m^{-3}$. Figure 2.6 reports the contours of constant nucleation rate coefficient for ML-mW obtained from FFS, along with data from the linear cooling rate simulations. Given the uncertainty of these values, the two methods show good agreement.

2.3 Direct MD

To confirm the validity of FFS and constant cooling rate simulations as methods of obtaining homogeneous nucleation rates, we explicitly compare thesm with direct MD simulation at a fixed temperature and pressure where spontaneous nucleation becomes accessible to direct MD. We choose the condition to be at 227 K, -500 atm, guided by the calculated ice nucleation rate based on FFS. We carry out 20 independent direct MD simulations using an isobaric-isothermal canonical ensemble, each lasting one micro second. From the distribution of induction time to ice nucleation (t_{ind}), defined as the time taken to form a critical ice nucleus, we obtain the distribution of probability for the system remaining liquid $P_{\mathrm{liq}}(t)$. Following the procedure described in Cox et al [34], we fit the calculated $P_{\mathrm{liq}}(t)$ by the following equation:

$$P_{\mathrm{liq}}(t) = \exp[-(Rt)^{\gamma}], \tag{2.1}$$

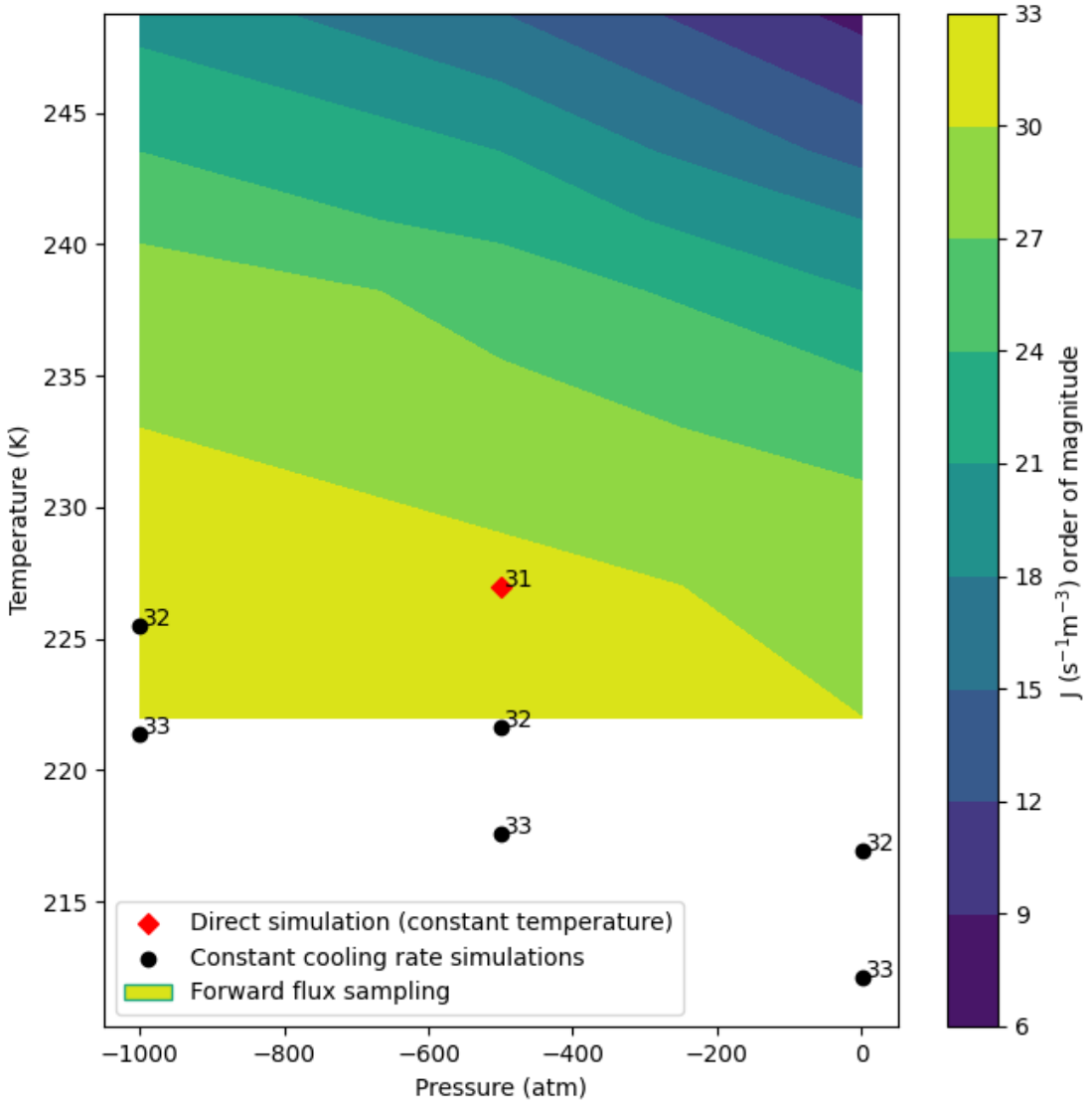

Figure 2.6: Contours of constant nucleation rate coefficient for the ML-mW model from forward flux sampling simulations. The black points are data from constant cooling rate simulations, labeled with the nucleation rate coefficient order of magnitude. The red data point is from direct MD simulation at constant temperature and pressure. The data sets are self consistent and the contour lines are roughly linear.

where R is nucleation rate and γ is fitting constant, as shown in Figure 2.7. The fitted ice nucleation rate R for this condition is found to agree well with the FFS

calculations, giving a nucleation rate coefficient of $6.93 \pm 0.13 \times 10^{31}$ m^{-3}s^{-1}, compared to $3.07 \pm 1.5 \times 10^{31}$ m^{-3}s^{-1} from FFS. This data point is plotted on Figure 2.6 (red), confirming the self-consistency of our methods.

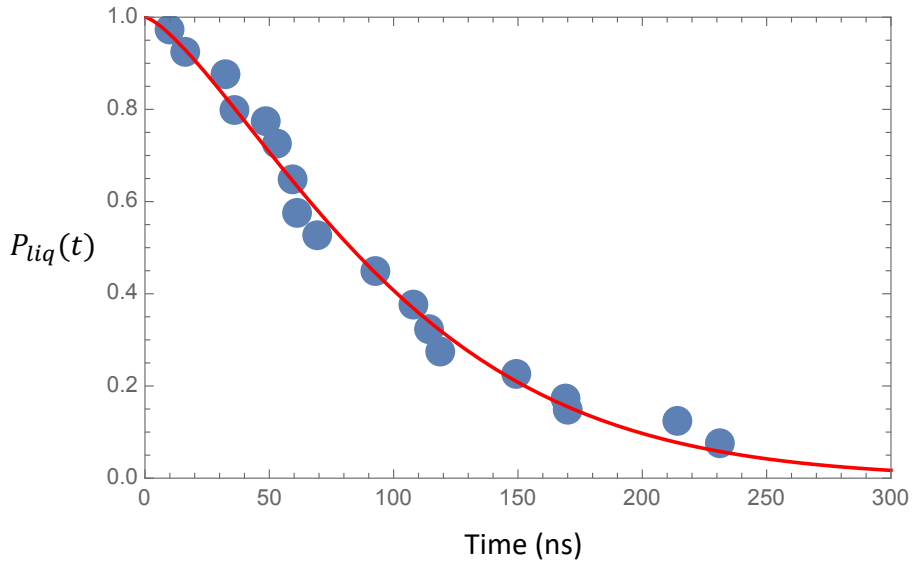

Figure 2.7: Ice nucleation rate R is obtained by fitting the calculated $P_{\mathrm{liq}}(t)$ (blue dots) by Eqn. 2.1. The fitted distribution is represented by the red line.

Chapter 3

Approximating the slope of constant nucleation rate lines

The performance of the ML-mW model is summarized by Chan et al. [14]. As acknowledged there, the improvement in Δv_{ls} results in an improved representation of the melting point line, $(dp/dT)_{melt}$ [14]. From the Clausius-Clapeyron relation, $(dp/dT)_{melt} = \Delta s/\Delta v_{ls}$, it is clear that the model's improvement in Δv_{ls} is primarily responsible for the improved behavior. The change in entropy upon melting, Δs, is the same within 5% between the two models, whereas the change in volume upon melting, Δv_{ls}, differs by roughly 230% between the two models. In this study, we analyze our simulation results in the context of Equation 1.1, leading us to conclude that an accurate representation of Δv_{ls} will also result in a more accurate representation of constant homogeneous nucleation rate lines, $(dp/dT)_{J=const}$.

An approximate expression of nucleation enhancement with decreasing pressure is proposed by Equation 1.1. Its derivation is outlined in this chapter. Starting from a reference point (p_0, T_0) with a known nucleation rate coefficient J, we look for p, T coordinates where this rate coefficient remains constant. By equating $J(p_0 + \Delta p, T_0 + \Delta T) = J(p_0, T_0)$, we arrive at an equation for lines of constant J in terms of pressure and temperature.

3.1 Derivation

When considering the behavior of homogeneous nucleation as a function of pressure, we can look at two effects: an elevation of the melting point, and a lowering of the Gibbs free energy barrier to nucleation. If one assumes that the level of supercooling needed to achieve a given nucleation rate coefficient remains fixed as one moves to lower pressures, then the elevated melting point alone leads to an equivalent elevation in the temperature corresponding to a given nucleation rate coefficient. However, the level of supercooling required is also expected to decrease due to a lowering of the Gibbs free energy barrier to nucleation:

$$\Delta G^* = \frac{16\pi\gamma_{ls}^3}{3(\rho\Delta\mu)^2}. \tag{3.1}$$

In this expression, ρ is the ice density, γ_{ls} is the solid-liquid interfacial energy, and $\Delta\mu$ is the change in chemical potential between the solid and liquid.

3.1.1 Pressure dependence of the chemical potential difference $\Delta\mu$

When the pressure of water is decreased, the nucleation rate is lowered due to a change in the chemical potential difference between liquid water and ice. Deriving a pressure-dependent formulation of the chemical potential difference between ice and liquid water under isothermal conditions, Němec 2013 arrives at the following expression [35]:

$$\mu_s - \mu_l = (p - p_{e,s})v_s - (p - p_{e,l})\frac{v_l(p) + v_l(p_{e,l})}{2} - kT\ln\left(\frac{p_{e,l}}{p_{e,s}}\right). \tag{3.2}$$

The derivation can be found in Equations 2-5 of Němec 2013 [35]. The value of $\mu_s - \mu_l$ that is obtained is for the given pressure p. The molecular volumes (m^3) for ice and liquid water are denoted by v_s and v_l. Note that in the present work, we use molar volumes ($cm^3\ mol^{-1}$). Equation 3.2 is derived in reference to known values for μ_s and μ_l at their equilibrium vapor pressures $p_{e,s}$ and $p_{e,l}$ respectively. This reference value is given as the third term on the right hand side of the equation, with the preceding terms interpreted as a change due to pressure. We substitute the ratio of equilibrium vapor pressures over supercooled liquid and ice with the commonly used expression from the Clausius-Clapeyron equation [36]

$$\frac{p_{e,l}}{p_{e,s}} = \exp\left(\frac{l_f}{RT_m}\frac{(T_m - T)}{T}\right). \tag{3.3}$$

where l_f is the enthalpy of fusion, assumed to be a constant, and T_m is the equilibrium melting temperature at the pressure $p_{e,l}$. We also impose the assumption that $(p - p_{e,s}) \approx (p - p_{e,l})$. This is valid because the values of p that we are investigating are on the order or 10 - 100 MPa, many orders of magnitude larger than the maximum difference $p_{e,l} - p_{e,s}$ seen in water (roughly 3×10^{-5} MPa). This approximation, combined with the substitution of Equation 3.3 gives us the following form, now expressed in terms of moles instead of per molecule:

$$\mu_s - \mu_l = (p - p_{e,l})\left[(v_s - v_l(p_{e,l})) - \frac{1}{2}(v_l(p) - v_l(p_{e,l}))\right] - \frac{l_f(T_m - T)}{T_m}. \tag{3.4}$$

From here we shall make some adjustments to the equation to suit our needs. First, we identify $p_{e,l}$ to be our reference pressure p_0, and $\Delta p = p - p_0$. We substitute $\Delta v_{ls} = v_l(p_0) - v_s$ and define $\Delta\mu = \mu_l - \mu_s$:

$$\Delta\mu = \Delta p\left(\Delta v_{ls} + \frac{1}{2}(v_l(p) - v_l(p_0))\right) + \frac{l_f(T_m - T)}{T_m}. \tag{3.5}$$

Lastly, we make the approximation that $\frac{1}{2}(v_l(p) - v_l(p_0)) \approx 0$. In other words, we make

the assumption that v_l is a constant, independent of pressure. In actuality, the value of v_l increases as the pressure decreases, due to water becoming less dense and closer in density to ice. This pressure dependence in v_l may explain the slight nonlinearity of temperature–pressure contours in Figure 2.6. To better approximate the observations, the $v_l(p) - v_l(p_0)$ term needs to be kept. To reasonable approximation we can ignore this dependence. Thus we arrive at the following approximation for the difference in chemical potential between supercooled liquid and solid, accounting for a pressure change:

$$\Delta\mu = \frac{l_f(T_m - T)}{T_m} + \Delta p \Delta v_{ls}. \tag{3.6}$$

This relation works well when T is close to T_m and the temperature dependence of l_f can be neglected. Higher order terms should be included when T is much lower than T_m.

According to Equation 3.6, as long as Δv_{ls} is negative, a decrease in pressure will increase $\Delta\mu$ at any given temperature, lowering the magnitude of ΔG^* (Equation 3.1). This in turn increases the nucleation rate. We note that the value of Δv_{ls} decreases with decreasing pressure and is expected to eventually reach an inflection point where it switches sign [12], so this proposed enhancement in nucleation rate due to Δv_{ls} is confined to the negative-pressure range where Δv_{ls} remains negative,

approximately the pressure range of this study.

3.1.2 Finding the slope $\Delta p/\Delta T$ for lines of constant nucleation rate

The chemical potential difference contributes to the Gibbs free energy barrier to nucleation, and the nucleation rate coefficient can be written as

$$J = A \exp\left(\frac{C}{T\Delta\mu^2}\right), \tag{3.7}$$

with $C = 16\pi\gamma_{ls}^3/(3k_B\rho^2)$. In this derivation, we assume that surface tension (γ_{ls}), density (ρ), and kinetic prefactor (A) remain constant for small changes in temperature and pressure. Starting from reference point $J(p_0, T_0)$, we aim to find an expression for lines of constant nucleation rate in temperature–pressure coordinates:

$$J(p_0 + \Delta p, T_0 + \Delta T) = J(p_0, T_0). \tag{3.8}$$

We use equations 3.6 and 3.7 in the above expression to solve for the slope ($\Delta p/\Delta T$) of the constant nucleation rate lines. Because we have taken A and all terms in C to be constant, they are eliminated from both sides of the expression. Taking the

logarithm of both sides, we have

$$(T_0 + \Delta T)\left(\frac{l_f(T_m - T_0 - \Delta T)}{T_m} + \Delta p \Delta v_{ls}\right)^2 = T_0\left(\frac{l_f(T_m - T_0)}{T_m}\right)^2. \tag{3.9}$$

Next we divide both sides by T_0 and make the approximation that $(T_0 - \Delta T)/T_0 \approx 1$. After taking the square root of both sides and rearranging, the resulting relation is

$$\frac{\Delta p}{\Delta T} = \frac{l_f}{T_m \Delta v_{ls}} \tag{3.10}$$

Using $\Delta p = p - p_0$ and $\Delta T = T - T_0$, we can use the slope to express a linear relation given as Equation 1.1

$$p(T) = p_0 + \frac{l_f}{T_m \Delta v_{ls}}(T - T_0)$$

Overall, the derivation is valid in the regime of linear response where the change of T or p is small and can be considered as small perturbation. It may also work in a greater range of (T, p) change, depending on the linearity of the melting line.

3.2 Comparing predictions with simulation results

Next we wish to compare the simulation results with Equation 1.1. For reference values p_0 and T_0, we use the temperature corresponding to $J = 10^{32}$ $\mathrm{m}^{-3}\mathrm{s}^{-1}$ at 1 atm, obtained from our constant cooling rate simulations. We input into Equation 1.1 the values we obtained for T_m and Δv_{ls}, and the value for l_f that is published in Chan et al. at 1 atm [14]. Equation 1.1 can then be used to predict the line of constant $J = 10^{32}$ $\mathrm{m}^{-3}\mathrm{s}^{-1}$ at negative pressures. The dashed lines in Figure 2.5 show the resulting expressions plotted along with the simulation results, showing satisfactory agreement in the pressure regime of interest. We find that this simple linear approximation gives reliable estimates of freezing point elevation under negative pressures in this pressure range. We note that the contours in Figure 2.6 are roughly linear as well, indicating that this trend remains consistent for smaller nucleation rate coefficients and lower supercooling.

Our simulation data indicate that within our error bounds, the equilibrium melting line and iso-nucleation rate lines are nearly parallel. The slope given by Equation 3.10 is parallel to the melting point line, despite the fact that the melting point line is known to not be the only mechanism contributing the shape of constant nucleation rate lines. A molecular dynamics study by Espinosa et al observed that γ_{ls} increases in response to strongly positive pressures, dominating the trend in G^* and causing

lines of constant nucleation rate to differ significantly in slope from that of the melting point line [37]. Experiments by Kanno et al at positive pressures have also shown that the nucleation rate line and melting point line are not parallel [25]. We expect our results can still be consistent with the results of these studies, because both of the aforementioned studies explore extreme positive pressures. We expect that in the negative pressure regime we explore, lines of constant nucleation rate are more similar in slope to the melting point line than at strongly positive pressures. For example, while Kanno et al's experimental results clearly show that the melting and freezing point lines are not parallel throughout the full range of positive pressures, the results indicate they are nearly parallel at the lower end of the pressure spectrum [25]. Section 3.4 discusses the findings of Espinosa et al [37]. There we describe how the agreement between Equation 1.1 and our data suggests that approximating γ_{ls} is valid in this range of pressures, for these models.

The finding that the enhancement in nucleation rate due to negative pressure can be approximated by Equation 1.1 will be helpful in future studies of ice nucleation at negative pressures, and in designing laboratory experiments to further explore this phenomenon. An important result is that pressure and temperature can each be modified independently to achieve a given nucleation rate enhancement. The apparent equivalence between temperature and pressure in influencing nucleation rates is a useful perspective in studying atmospheric ice nucleation, for which focus has been placed primarily on the effect of temperature on nucleation rates with pressure held

constant. This work provides further tools for the continued investigation of pressure fluctuations as an ice nucleation mechanism.

3.3 The role of the Density Anomaly

We have identified that the density anomaly Δv_{ls} is a key factor in determining the shape of the melting point line and also influences the change in Gibbs free energy barrier with pressure through its impact on $\Delta\mu$. Given that the ML-mW model exhibits a density anomaly roughly 230% larger than that of the mW model, our expectation is that decreasing pressure will have a much more significant influence on the nucleation rate in the ML-mW model over the mW model. When comparing our results for the two models, we do indeed observe that the slope $(dP/dT)_{J=const}$ is larger for the ML-mW model. As shown in Figure 2.5, the ML-mW model shows a larger increase in homogeneous nucleation rate coefficient for the same decrease of pressure. This analysis leads to our conclusion that the improved density anomaly makes ML-mW better equipped for studying ice nucleation in the context of changing pressures. When using a water model with a small density anomaly compared to real water, one may not capture the effects of pressure change on ice nucleation that would be exhibited in real water.

No experimental freezing measurements for water at negative pressure exist to our

knowledge. We therefore cannot directly compare the nucleation rate trend that results from improvement in Δv_{ls} with the nucleation rate behavior of real water, but for the following reasons we think higher fidelity to the iso-nucleation lines of real water will happen as a result of improved Δv_{ls}.

Equation 1.1, indicates that Δv_{ls} contributes directly to the slope of constant nucleation rate lines in water. This equation shows satisfactory agreement with our simulation data, which do not rely on theory in obtaining nucleation rate coefficients. Therefore, we draw the conclusion that Equation 1.1 is reliable for predicting constant nucleation rate lines for the ML-mW and mW water models. The role of Δv_{ls} in Equation 1.1 implies that an improvement in Δv_{ls} must heavily contribute to the accuracy of the water model in producing constant nucleation rate lines. We can further justify the role of Δv_{ls} in this improvement because it is the variable that changes most dramatically between the two models. Between the two water models, l_f changed by 10%, T_m changed by 7%, and Δv_{ls} changed by 228.5%.

This specific mechanism of enhanced ice nucleation that we are exploring is limited to the range of pressures where Δv_{ls} is negative and contributes to a decrease in chemical potential difference as pressure is lowered. Therefore, the pressure range used in this study is selected as the approximate range where Δv_{ls} is expected to be negative. Bianco et al [12] shows a peak in the curve of the homogeneous nucleation rate in TIP4P at around -1000 atm, which is caused by the density anomaly switching sign.

In our study, we also notice the density of ice and liquid converging as we approach -1000 atm.

Table 3.1 reports Δv_{ls} values that we have computed for the mW and ML-mW models at their equilibrium melting temperatures at 1 atm, -500 atm, and -1000 atm. The values were determined by measuring the molar volume (cm^3 mol^{-1}) of an equilibrated box of liquid containing $\sim$ 4100 water molecules and separately measuring the molar volume of equilibrated ice at the same temperature and pressure. We take the difference between these values to obtain Δv_{ls}. The values we report at 1 atm are in agreement with published values in Chan et al. [14].

Table 3.1
Δv_{ls} ($cm^3 mol^{-1}$) at liquid-solid coexistence temperature for ML-mW model and original mW model at negative pressures

Pressure (atm)	ML-mW	mW	Experiment
1	-1.35	-0.42	-1.61 [14]
-500	-1.17	-0.35	
-1000	-0.95	-0.27	

The values of Δv_{ls} decrease with pressure along the melting point line, but remain negative in the pressure range that we study. We also note that the change in Δv_{ls} with pressure is much smaller than the change in Δv_{ls} between the two water models. In this pressure range, the shape of the constant nucleation rate lines are linear to first order approximation, but higher order approximations would include the change in Δv_{ls} with pressure.

3.4 Sources of error and limitations

Despite the various ways that the Gibbs free energy barrier is affected by decreasing pressures, our simulation results indicate that a linear approximation for the slope of constant nucleation rate lines can provide an excellent first order approximation in the pressure range that is studied in this work. Because it leaves out some important physical processes, it is not an exact expression. Here we discuss additional factors which would need to be included in a higher order approximations of the iso-nucleation rate lines.

3.4.1 Interfacial free energy γ_{ls}

Section 3.2 discussed our finding that lines of constant nucleation rate are roughly parallel to the melting point line in our pressure regime, indicating that approximating γ_{ls} as constant is suitable in this pressure regime. However, given that γ_{ls} is cubed in Equation 3.1, approximating it as constant is likely to be a primary source of error in our linear approximation and merits careful consideration.

Our simulation results indicate that the change in γ_{ls} along constant nucleation rate lines may not be as pronounced in the negative pressure regime as at extreme positive

pressures. This speculation comes from the fact that Espinosa et al. [37] identified γ_{ls} as the main factor in changing the constant nucleation rate slope relative to the melting point line. However, our simulation results do not show a dramatic deviation between the two slopes, indicating that the contribution from γ_{ls} pressure dependence is less pronounced.

In the derivation of Equation 1.1, we find lines of constant nucleation rate by setting $J(p_0 + \Delta p, T_0 + \Delta T)$ equal to $J(p_0, T_0)$. In order to move forward with our derivation, we assume that surface energy γ_{ls} remains constant along lines of constant nucleation rate, allowing us to eliminate the γ_{ls}^3 term from both sides of the equality. The agreement in slopes we observe suggest that this is a reasonable approximation in the range considered. From Espinosa et al. [37], we see that γ_{ls} decreases as pressure is lowered, and increases as temperature is raised. Therefore, as we move to higher temperatures and lower pressures along lines of constant nucleation rate, these two effects partially compensate for each other. We expect that this behavior mitigates the error introduced in our derivation of Equation 1.1.

An important outcome of this analysis is that the relative change in γ_{ls} with temperature and pressure impacts the accuracy of the linear approximation given by Equation 1.1 because it determines how much γ_{ls} changes along lines of constant nucleation rate. Figure 1(d) of Espinosa et al. [37] shows that for the TIP4P/Ice water model, γ_{ls} increases by roughly 10 mJ/m^2 due to a 2000 atm increase in pressure,

and decreases by roughly 10 mJ/m^2 from a 40 K decrease in temperature. However, given that Espinosa et al. considers only two pressures, 1 atm and 2000 atm, it is possible that surface energy is not a linear function of pressure, such that it undergoes a smaller variation in the narrower pressure range (1 atm to -1000 atm) that we are studying. To our knowledge, the pressure dependence of γ_{ls} is not known experimentally, nor has a pressure dependent theoretical expression been proposed. By combining Equation 3.6 with Equation 5 of Espinosa et al. [37], one could attempt to formulate such an expression.

3.4.2 Enthalpy of fusion and other factors

The enthalpy of fusion is another term that contributes to the slope of $\Delta p/\Delta T$. We do not compute the enthalpy of fusion at negative pressures. It is generally accepted that enthalpies of phase transitions depend weakly on temperature, for example Bohren and Albrecht [36], Chapter 5.3 explains that over narrow temperature ranges enthalpy of phase changes can be taken as constant, but for higher accuracy they can be considered a linear function of temperature. To our knowledge, the pressure dependence of the enthalpy of fusion is not known experimentally, nor has a pressure dependent theoretical expression been derived.

Despite experimental and theoretical uncertainty around the pressure dependence

of each variable taken as constant along lines of constant J, we have shown that approximating them as constants results in satisfactory agreement with simulation results. It is possible that some of these variables increase along lines of constant J while others decrease, resulting in fortuitous cancellation of errors.

The motivation of this study is to establish an expression that can be used for investigating a mechanism of increased nucleation rate, without decreasing the temperature. The pressure range used in this study is selected as the range where Δv_{ls} is expected to contribute to an increase in nucleation rate as pressure decreases, as well as a pressure range that is feasibly achieved in atmospheric or experimental context. This justifies our limited range of conditions where this expression can be valid.

As can be seen in Figure 2.5 of this document, the linear approximation of Equation 1 becomes less representative of the observed curve as we move further from the reference point at 1 atm. However, given that experimental measurements of homogeneous freezing are limited to atmospheric pressures, we believe this can provide a useful expression for predicting the increase in nucleation rate one might expect from negative pressures, particularly in atmospheric applications or in designing of future experimental setups to investigate this phenomenon further. This work aims to establish a simple, linear expression for the iso-nucleation rate lines at negative pressures for such applications.

Chapter 4

Conclusions

We used MD simulation to evaluate homogeneous ice nucleation rate coefficients in a range of negative pressures, by means of constant cooling rate simulations as well as forward flux sampling. We compare the effect of negative pressure on nucleation rate coefficients between the ML-mW and the original mW model, concluding that the density difference between water and ice is a dominant factor in determining the extent to which nucleation rates in these models are increased when negative pressure (stress) is applied to the system. Based on this analysis, the ML-mW model is more appropriate than the original mW model for simulations involving ice nucleation at different pressures.

We obtained freezing temperature distributions for both water models at each pressure, which are then converted to nucleation rate coefficients. Lines of constant nucleation rate coefficient in pressure–temperature coordinates verify that a linear approximation can be used to predict the enhancement in nucleation rate due to negative pressure in the pressure range that is studied.

References

[1] Marcolli, C. *Scientific Reports* **2017**, *7*.

[2] Yang, F.; Cruikshank, O.; He, W.; Kostinski, A.; Shaw, R. *Physical Review E* **2018**, *97*, 023103.

[3] Maeda, N. *Molecules* **2021**, *26*(2), 392.

[4] Murray, B.; O'sullivan, D.; Atkinson, J.; Webb, M. *Chemical Society Reviews* **2012**, *41*(19), 6519–6554.

[5] Dorsey, N. E. *Transactions of the American Philosophical Society* **1948**, *38*(3), 247–328.

[6] Nalesso, S.; Bussemaker, M. J.; Sear, R. P.; Hodnett, M.; Lee, J. *Ultrasonics sonochemistry* **2019**, *57*, 125–138.

[7] Yang, F.; Shaw, R. A.; Gurganus, C. W.; Chong, S. K.; Yap, Y. K. *Applied Physics Letters* **2015**, *107*, 264101.

[8] Niehaus, J.; Cantrell, W. *The Journal of Physical Chemistry Letters* **2015**, *6*, 3490–3495.

[9] Roedder, E. *Science* **1967**, *155*(3768), 1413–1417.

[10] Yang, F.; Cantrell, W. H.; Kostinski, A. B.; Shaw, R. A.; Vogelmann, A. M. *Atmosphere* **2020**, *11*(1).

[11] Li, T.; Donadio, D.; Galli, G. *Nature Communications* **2013**, *1887*.

[12] Bianco, V.; de Hijes, P. M.; Lamas, C. P.; Sanz, E.; Vega, C. *Phys. Rev. Lett.* **2021**, *126*, 015704.

[13] Molinero, V.; Moore, E. *The Journal of Physical Chemistry B* **2009**, *113*, 4008–4016.

[14] Chan, H.; Cherukara, M. J.; Narayanan, B.; Loeffler, T. D.; Benmore, C.; Gray, S. K.; Sankaranarayanan, S. K. R. S. *Nature Communications* **2019**, *10*, 2009–2014.

[15] Allen, R. J.; Frenkel, D.; Ten Wolde, P. R. *J Chem Phys* **2006**, *124*(2), 024102.

[16] Espinosa, J. R.; Sanz, E.; Valeriani, C.; Vega, C. *The Journal of Chemical Physics* **2014**, *141*, 18C529.

[17] Plimpton, S. March **1995**, *117*(1), 1–19.

[18] Johnston, J. C.; Molinero, V. *Journal of the American Chemical Society* **2012**, *134*(15), 6650–6659.

[19] Steinhardt, P. J.; Nelson, D. R.; Ronchetti, M. *Physical Review B* **1983**, *28*, 784–805.

[20] Lupi, L.; Hudait, A.; Molinero, V. *Journal of the American Chemical Society* **2014**, *136*, 3156–3164.

[21] Zobrist, B.; Koop, T.; Luo, B. P.; Marcolli, C.; Peter, T. *The Journal of Physical Chemistry C* **2007**, *111*(5), 2149–2155.

[22] Koop, T.; Luo, B.; Biermann, U. M.; Crutzen, P. J.; Peter, T. *J. Phys. Chem. A* **1997**, *101*, 1117–1133.

[23] Heneghan, A. F.; Haymet, A. D. J. *The Journal of Chemical Physics* **2002**, *117*(11), 5319–5327.

[24] Shaw, R. A.; Durant, A. J.; Mi, Y. May **2005**, *109*(20), 9865—9868.

[25] Kanno, H.; Speedy, R. J.; Angell, C. A. *Science* **1975**, *189*(4206), 880–881.

[26] Espinosa, J. R.; Sanz, E.; Valeriani, C.; Vega, C. *The Journal of Chemical Physics* **2013**, *139*, 144502.

[27] García Fernández, R.; Abascal, J. L. F.; Vega, C. *The Journal of Chemical Physics* **2006**, *124*, 144506.

[28] Li, T.; Donadio, D.; Russo, G.; Galli, G. November **2011**, *13*(44), 19807–19813.

[29] Haji-Akbari, A.; DeFever, R. S.; Sarupria, S.; Debenedetti, P. G. *Phys Chem Chem Phys* **2014**, *16*(47), 25916–25927.

[30] Haji-Akbari, A.; Debenedetti, P. G. August **2015**, *112*(34), 10582–10588.

[31] Cabriolu, R.; Li, T. May **2015**, *91*, 052402.

[32] Lupi, L.; Peters, B.; Molinero, V. December **2016**, *145*(21), 211910.

[33] Lupi, L.; Hudait, A.; Peters, B.; Grünwald, M.; Mullen, R. G.; Nguyen, A. H.; Molinero, V. November **2017**, *551*(7679), 218–222.

[34] Cox, S. J.; Kathmann, S. M.; Slater, B.; Michaelides, A. *The Journal of Chemical Physics* **2015**, *142*(18), 184704.

[35] Němec, T. *Chemical Physics Letters* **2013**, *583*, 64–68.

[36] Bohren, C. F.; Albrecht, B. A. *Atmospheric thermodynamics;* Oxford University Press: New York, 1988.

[37] Espinosa, J. R.; Zaragoza, A.; Rosales-Pelaez, P.; Navarro, C.; Valeriani, C.; Vega, C.; Sanz, E. Sep **2016**, *117*, 135702.

[38] Fortunato, S. *Phys. Rep.-Rev. Sec. Phys. Lett.* **2010**, *486*, 75–174.

[39] Li, T.; Donadio, D.; Ghiringhelli, L. M.; Galli, G. *Nature Materials* **2009**, *8*, 726–730.

[40] Bi, Y.; Cao, B.; Li, T. *Nat. Comm.* **2017**, *8*.

[41] Sanz, E.; Vega, C.; Espinosa, J. R.; Caballero-Bernal, R.; Abascal, J. L. F.; Valeriani, C. *Journal of the American Chemical Society* **2013**, *135*, 15008–15017.

[42] Thompson, A. P.; Plimpton, S. J.; Mattson, W. *The Journal of Chemical Physics* **2009**, *131*, 154107.

[43] Gurganus, C. W.; Charnawskas, J. C.; Kostinski, A. B.; Shaw, R. A. Dec **2014**, *113*, 235701.

[44] Davis, R. D.; Lance, S.; Gordon, J. A.; Ushijima, S. B.; Tolbert, M. A. *Proceedings of the National Academy of Sciences* **2015**, *112*(52), 15815–15820.

[45] Vega, C.; Sanz, E.; Abascal, J. L. F.; Noya, E. G. mar **2008**, *20*(15), 153101.

[46] Huang, J.; Bartell, L. S. *The Journal of Physical Chemistry* **1995**, *99*(12), 3924–3931.

Appendix A

Equilibrium melting temperature

The data points for the melting point line in Figure 2.5 are obtained by using the direct-phase coexistence method at each pressure, where the melting temperature is taken as the lowest temperature where the system completely melts [26] [27]. Figure A.1 shows our results at 1 atm for the two water models. We can use our 1 atm result as validation. While our outcome for the mW model precisely matches published results of 273 K, we find that our outcome for ML-mW (292 K) is different from the published value by Chan et al. [14] for the melting temperature of ML-mW (289 K). Chan et al. [14] used a different method than used here, but other work has shown that these two methods typically agree [45], so the discrepancy is at this point unexplained. Nevertheless, for this study we are not concerned with the exact value of the melting point, but the relative changes with respect to pressure, and the qualitative behavior of the freezing point relative to the melting point.

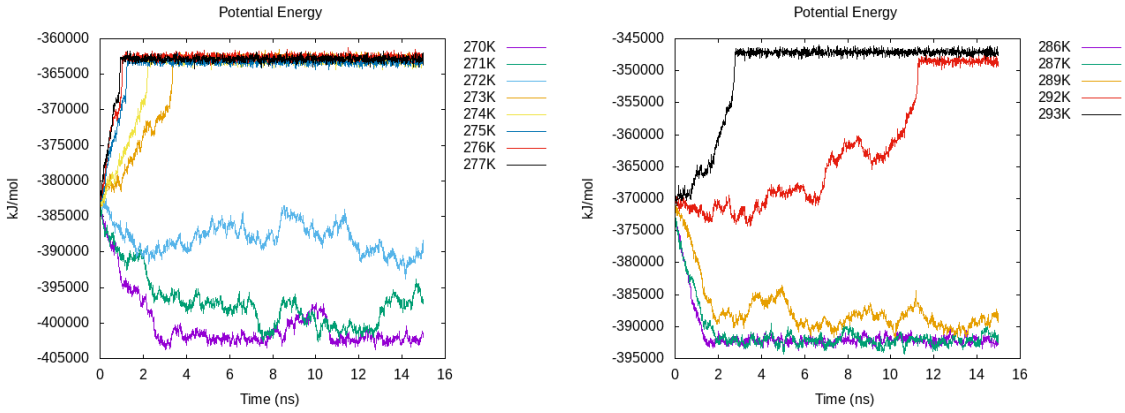

Figure A.1: Left: Original mW model potential energy trajectories at 1 atm, showing the system melting at temperatures equal or greater than 273K. Right: ML-mW model potential energy trajectories at 1 atm, showing the system melting at temperatures equal or greater than 292K.

The results of the method are summarised in Table A.1. The uncertainty on the

reported values are ±1K.

Table A.1
Melting temperatures of ML-mW model and original mW model at negative pressures

Pressure (atm)	ML-mW (K)	mW (K)	Experiment (K)
1	292	273	273
−500	295	274	
−1000	298	275	279 [1]

Appendix B

Convergence of Forward Flux Sampling calculations

This Appendix material is contributed by Tianshu Li.

To validate the convergence of FFS calculation with respect to the number of configurations (N_i) collected at each interface λ_i, we repeat FFS calculations under two conditions, *i.e.*, 227 K, -500 atm and 233 K, 1 atm, by collecting 1,000 configurations at each interface. The calculated rates are compared against with those computed using 600 configurations, based on three independent FFS runs each collecting 200 configurations. As shown in Table B.1, the calculated rates are virtually unchanged with respect to the number of collected configurations, demonstrating the convergence of rate constants calculated by FFS.

Table B.1
Comparison of the calculated ice nucleation rates ($m^{-3}s^{-1}$) using FFS for different numbers of configurations

Method	227 K, -500 atm	233 K , 1 atm
FFS (600 configurations)	$3.72 \pm 0.97 \times 10^{31}$	$3.00 \pm 0.43 \times 10^{26}$
FFS (1,000 configurations)	$3.07 \pm 1.5 \times 10^{31}$	$1.54 \pm 0.62 \times 10^{26}$